Large Eddy Simulation of Transitional Boundary Layer on Horizantal Axis Wind Turbine Blade

Zhenrong Jing, Antoine Ducoin, Caroline Braud

Direct numerical simulation of transitional boundary layers on a horizontal axis wind turbine blade

Direct numerical simulation of transitional boundary layers on a horizontal axis wind turbine blade

Z Jing, A Ducoin and C Braud

LHEEA, Ecole Centrale Nantes, 1 Rue de la No, 44321 Nantes, France.

E-mail: antoine.ducoin@ec-nantes.fr

Abstract. In boundary layer flow around rotating machines, a radial (or cross-flow) velocity exists due to Coriolis and centrifugal forces. This velocity component can be of great importance for laminar-turbulent transition. A series of direct numerical simulations (DNS) are performed to study the boundary layer flow transition on a rotating Horizontal Axis Wind Turbine blade. To quantify the effect of blade rotation, results are compared with that from airfoil DNS, where the section is taken from 3D blades and does not rotate. It is shown that the rotation gives rise to a small radial velocity and slightly modifies the shape of unstable waves. However, the transition location and mechanism of 3D blade boundary layer flow resemble 2D flow for the investigated case.

1. Introduction

Horizontal Axis Wind Turbine (HAWT) blade consists of a series of 2D airfoil sections with different thicknesses, chord lengths, and twist angles. In the design and optimization of HAWT, Blade Element Theory (BET) is widely used. After dividing the blade into sections (or elements) in the spanwise direction, BET assumes that the flow around each section is locally 2-dimensional. The lift and drag forces for each section can be obtained from momentum theory or calculated from the code XFOIL [1]. The total torque of the blade can be then obtained by summing local sections' performance together [2][3].

Nonetheless, the flow around the HAWT blade is not strictly 2D. As early as 1945, Himmelskamp [4] has observed that the lift coefficient for the rotating blade is increased compared with the non-rotating case, and the stall is postponed. This phenomenon is referred to as *rotational augmentation* in the later literature. Nowadays, it is well recognized that rotational augmentation is closely related to the large radial velocities in flow separation regions. On one hand, the radial velocity *pump* fluid from separation region to radial direction, leading to volume reduction of separation bubble [5]. On the other hand, the radial velocity induces a streamwise Coriolis force, which partially counteracts the adverse pressure gradient [6].

The large radial velocity inside flow separation region is a result of flow deceleration in azimuthal direction. In figure 1 a blade is rotating in the plane (x, y), i.e., the angular velocity $\boldsymbol{\omega}$ of the rotating reference frame fixed to the blade is $(0, 0, \omega_z)$. Considering a fluid parcel at $\boldsymbol{r} = (r, \theta, z)$ (r, θ, z are radius, angle, and depth in cylindrical coordinate system respectively), its velocity relative to the rotating reference frame $\boldsymbol{U}$ is (u_r, u_θ, u_z). The centrifugal force $-\boldsymbol{\omega} \times (\boldsymbol{\omega} \times \boldsymbol{r})$ on this fluid parcel would be $(r\omega_z^2, 0, 0)$ (in local radial, azimuthal, and depth directions respectively) . And the Coriolis force $-2\boldsymbol{\omega} \times \boldsymbol{U}$ on it would be $(-2u_\theta\omega_z, 2u_r\omega_z, 0)$.

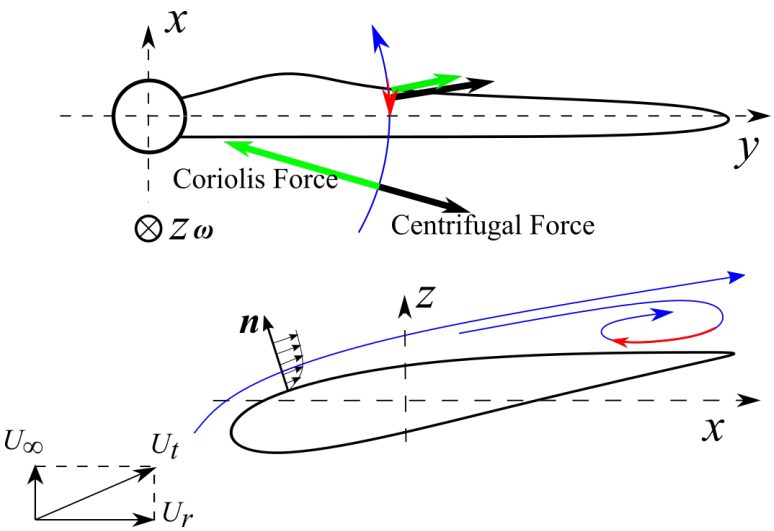

Figure 1: Inside the separation bubble, streamwise velocity changes its direction (red arrow), which causes the Coriolis force (green arrow) acts in the same direction as the centrifugal force (black arrow).

Far away from the blade, the fluid parcel experience circular motion with $u_\theta = r\omega_z$. The centripetal force needed for this circular motion is $(-r\omega_z^2, 0, 0)$, which is exactly the combination of centrifugal and Coriolis forces. When flow detaches, the azimuthal velocity decreases and reverses its direction. As a result, Coriolis force changes its direction and acts in the same direction as centrifugal force, which results in large radial velocity u_r.

Inside the attached boundary layer, the azimuthal velocity decreases because of the non-slip boundary condition (BC). As a result, Coriolis force decreases, and centrifugal force would pull the flow outward. This means a radial velocity appears in the attached boundary layer as in the separation regions. In fact, the cross-flow velocity in rotating disk boundary layer flow appears due to the same mechanism. Hereafter, we shall use radial and cross-flow velocities interchangeably. Since rotating disk boundary layer flow is a prototype flow for cross-flow instability [7], natural questions to ask are: can cross-flow instability happen on the rotating HAWT blade boundary layer? And how does rotation affect the laminar-turbulent transition on HAWT blade?

The laminar-turbulent transition of boundary layer flow can be of great importance for HAWT. It not only affects aerodynamic characteristics like lift and drag but also generates load fluctuations, which might decrease the rotor life. Much endeavor has been made to understand the flow transition on rotating blade boundary layer flows. Bosschers [8] pointed out that laminar-turbulent transition on a rotating blade might occur due to cross-flow. In the DanAero MW projects [9] [10], the transition location on a full-scale multi-megawatt turbine is derived from surface pressure fluctuations measured by microphones. The transition location on the pressure side is advanced as compared to wind tunnel experiments. This difference of transition locations is caused by different characteristics of incoming turbulence in wind tunnel and field measurements. Heister's [11] study of helicopter rotor shows there coexist multiple transition scenarios, including bypass transition, leading edge contamination, cross-flow transition, and Tollmien-Schlichting (TS) wave. Hernandez [12] performed linear stability theory (LST) analysis on rotating flat plate boundary layers to study the transition on HAWT. Although there is a cross-flow component in the base flow, his analysis is only restricted to TS waves. Weiss [13] measured the boundary layer transition on rotating blades by temperature-sensitive paint. He also performed LST analysis and found that the critical transition N-factor is around 8.4. Reichstein et al. [14] show that thermographic imaging can be used as a non-intrusive method for detecting flow transition on a multi-megawatt wind turbine. The transition location derived from thermographic imaging is in good agreement with results from microphones and transitional

Computational Fluid Dynamic (CFD) simulation. When the wind turbine is in regular operation mode, the flow transition appears quite near the leading edge ($x/c = 0.05$).

Although previous studies show that the radial flow is not dominant in attached boundary layer flow on rotating blade, it would still be helpful to have some quantitative information on it. Due to HAWT's large scale and unsteadinesses, accurate measurements of boundary layer profile and transition by experiments are of great challenge. On the other hand, CFD offers an feasible approach, which can get the full information of the flow field. To the best of authors knowledge, there is no numerical simulation which fully resolve boundary layer flow and captures the laminar-turbulent transition on rotating HAWT blade. This paper aims to provide a such study to better understand the boundary layer laminar-turbulent transition on HAWT blade.

2. Methodology

2.1. HAWT blade model

The model under investigation is the LM38.8 blade from the DanAero MW project, whose section is a series of NACA63-4XX profiles (XX is the maximum thicknesses). It has a 1.24-meter extension in the root, so the total span length R is 40.04 meter. The simulation parameters are taken from the first round of calculations of DanAero MW experiments: the incoming wind velocity U_∞ is uniform and equals to $6.1m/s$, the blade rotates with an angular velocity $\omega_z = 12.3rpm$. However, to make the simulation feasible, we reduced the Reynolds number by one order. For that purpose, the kinematic viscosity ν is set to $2 * 10^{-4}m^2/s$, which is about one order larger than that of air. The induction effect of the wind turbine is not taken into consideration in the present study. However, it can be included by changing the normal incoming velocity U_∞ to $9.15m/s$ if the induction factor $a = 0.33$ for the ideal wind turbine is used.

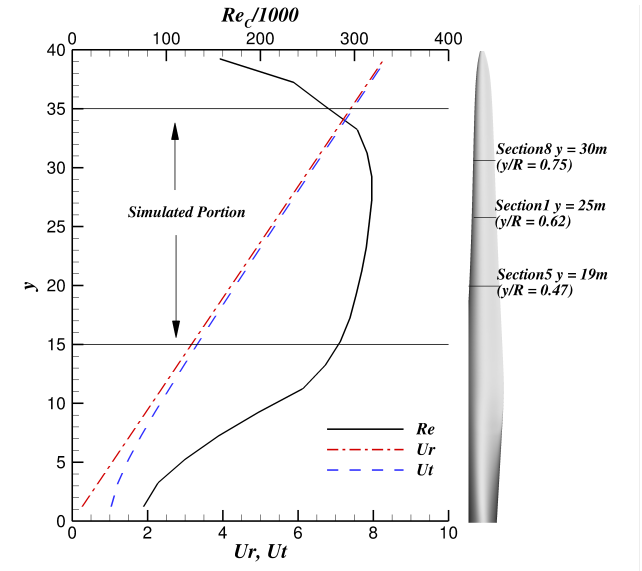

Figure 2: Variation of Re_c, U_r, U_t along the span (Velocities are normalized by U_∞).

During the simulations, the blade is kept stationary, whereas the blade rotation is taken into account by solving the Navier-Stokes equation in rotational reference frame. The coordinate system used is shown in figure 1. The blade's span direction is aligned with y axis. At each span section y, the local effective velocity U_t has two components: the velocity of wind U_∞, which is in z direction; and a component due to rotation $U_r = r\omega$, which is in $x - y$ plane. Figure 2 shows the variation of U_r and U_t along the span. The variation of chord Reynolds' number $Re_c = U_t c_l/\nu$ based on local chord length c_l is also ploted in the figure.

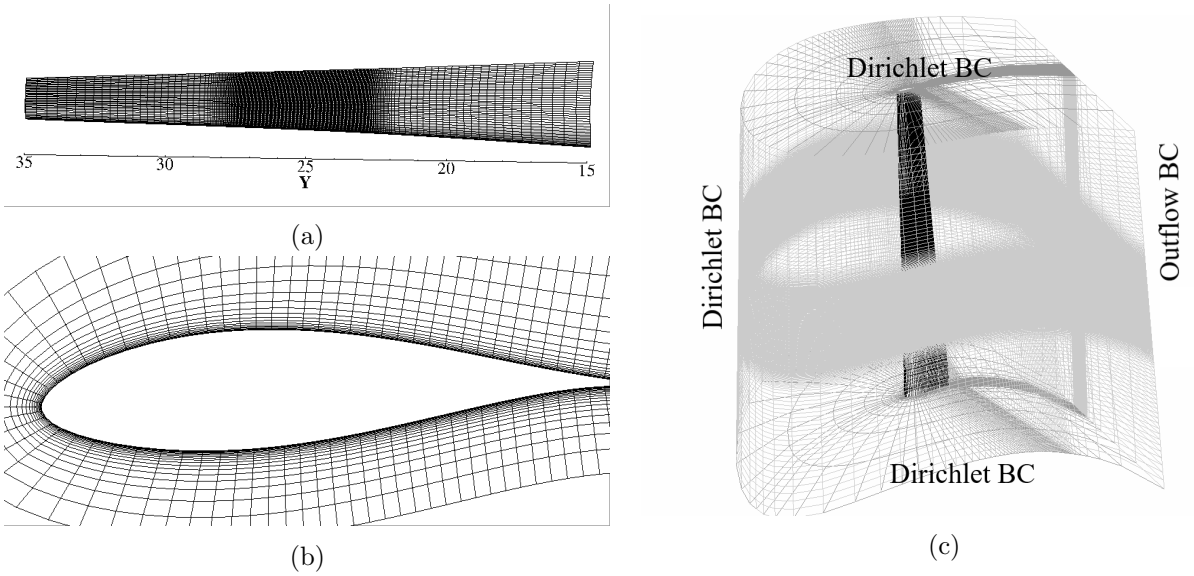

Figure 3: The mesh for the turbine blade

2.2. the mesh and boundary conditions

Even with the reduced Reynolds number, it is still impossible to resolve the whole blade with our computational capacity. So we restrict the simulation domain from $y = 15m$ to $y = 35m$, where the chord Reynolds' number is roughly constant (figure 2). For Section5 and Section8 marked in figure 2 (the names follow the convention in DanAero MW project), 2D airfoil (uniform span and without rotation) wind tunnel measurements of pressure coefficient C_p are also available for each section. In the simulation, 42 sensors are put along Section1 to record the variation of flow quantities with time.

Figure 3 shows the computational domain and mesh. As can be seen in figure 3a, the mesh in span direction is concentrated around the center of the blade. Local mesh refinement for the boundary layer is shown in figure 3b. There are 230 elements in span-wise direction, 25 elements in wall-normal direction, and 78 elememts around the airfoil in streamwise direction. The total element number is 0.67 million (wake mesh included), which means the total degree of freedom is 0.49 billion if order 10 is used in each element.

On the blade surface, non-slip wall BC is applied. Outflow BC is used on the vertical surface behind the trailing edge. Dirichlet BC is used for the surface around the blade. The BC on the two ends of span-wise direction is hard to define because the computational domain is truncated from a whole blade and the flow quantities on those boundaries are not known. We simply impose Dirichlet BCs on them. On all the Dirichlet BCs, the velocities at position (x, y, z) are specified as $U_x = \omega_z y$, $U_y = -\omega_z x$, and $U_z = U_\infty$, which are the sum of unperturbed rotation and wind velocities. A smaller domain simulation shows that the boundary conditions at two span ends have negligible influence on the flow in the center region.

2.3. Airfoil simulation

To better illustrate the effect of rotation, an airfoil simulation is also performed in this paper. The airfoil used is NACA63-420, which is the same as the LM38.8 blade section at $y_0 = 25.24m (y_0/R = 0.63)$. It is extruded to 1 meter in y direction (span-wise direction). Periodic BCs are used on the two span ends for this airfoil simulation. The incoming flow is uniform along the span and is the same as the local incoming flow at y_0 of the 3D blade case. Velocities on the Dirichlet boundary are specified as $U_x = \omega_z y_0$, $U_y = 0$, and $U_z = U_\infty$.

The mesh for the airfoil simulation is uniform in the span-wise direction and have a roughly same resolution as the 3D blade simulation. The blade rotation is not considered. When airfoil sections are tested in wind tunnels, it usually has a uniform span and does not rotate. The airfoil simulation serves the purpose of replicating wind tunnel experiments.

2.4. Solver

The Navier-Stokes equation in the rotating frame can be written as:

$$\nabla \cdot \boldsymbol{U} = 0$$
$$\frac{\partial \boldsymbol{U}}{\partial t} + \boldsymbol{U} \cdot \nabla \boldsymbol{U} + \underbrace{\boldsymbol{\omega} \times (\boldsymbol{\omega} \times \boldsymbol{r})}_{\text{Centrifugal term}} + \underbrace{2\boldsymbol{\omega} \times \boldsymbol{U}}_{\text{Coriolis term}} = -\nabla p + \nu \Delta \boldsymbol{U} \tag{1}$$

where $\boldsymbol{U} = \{U_x, U_y, U_z\}$ are the velocities in $\{x, y, z\}$ directions, $\boldsymbol{\omega}$ is the angular velocity vector of the rotating frame, $\boldsymbol{r}$ is the position vector and p is the pressure. Compared with the NS equation in the inertia frame, two additional terms arise because of rotation, namely centrifugal term and Coriolis term.

The above equation is solved by the open-source code NEK5000 [15], which is a scalable Spectral Element Method(SEM) solver. SEM is a hybrid method combining Finite Element Method and Spectral Method. After dividing the computational domain into elements, orthogonal polynomials are used as shape functions. For more information about NEK5000 and SEM, please refer to [16].

In high order methods like SEM, mesh convergence study and refinement can be done by increasing the order of spectrum in the elements (p refinement) instead of generating new mesh (h refinement). In this paper, we performed three simulations with spectrum order 6, 8, and 10. The simulations took around 2 million CPU-hours on the Turing machines of IDRIS. All the quantities are collected after the flow fields are statistically converged. For clarity, we omit the results for order 6 in the following section.

3. Results

The solver NEK5000 is based on the Cartesian coordinate. However, when *azimuthal* and *radial* velocities are refered to, the velocities in $x - y$ plane are transformed into the cylindrical coordinate system that shares the same z as the Cartesian frame. Obviously, without the blade, radial velocity u_r would be zero.

A proper local coordinate system is also needed when velocity profiles are concerned. In figure 1, $\boldsymbol{n}$ is the *wall-normal* direction of a point on the blade wall. *Streamwise* velocity is obtained by projecting azimuthal velocity and U_z to wall tangential direction (perpendicular to $\boldsymbol{n}$). The local radial velocity is the same as that in cylindrical coordinate. Another note is that all the velocities are normalized by the incoming flow velocity U_∞.

3.1. Flow field

Figure 4 shows the chord-wise C_p distribution at two sections. The chord Reynolds' number of wind tunnel experiments is 1.5 million, which is five times larger than the Re_c of the numerical simulations. However, when the Re_c is large, the boundary layer is thin enough to not affect C_p very much. An important observation from figure 4 is that the C_p of 3D simulation agrees well with both the airfoil simulation and the wind tunnel test. The rotating blade simulation C_p is almost the same as the airfoil simulation result (figure 4a). However, this is not against rotation augmentation because it only happens when there are large flow separations.

In figure 4b, two pressure plateaus are marked out on the numerical results. Pressure plateaus usually indicate flow separations at the corresponding locations. However, there is no pressure

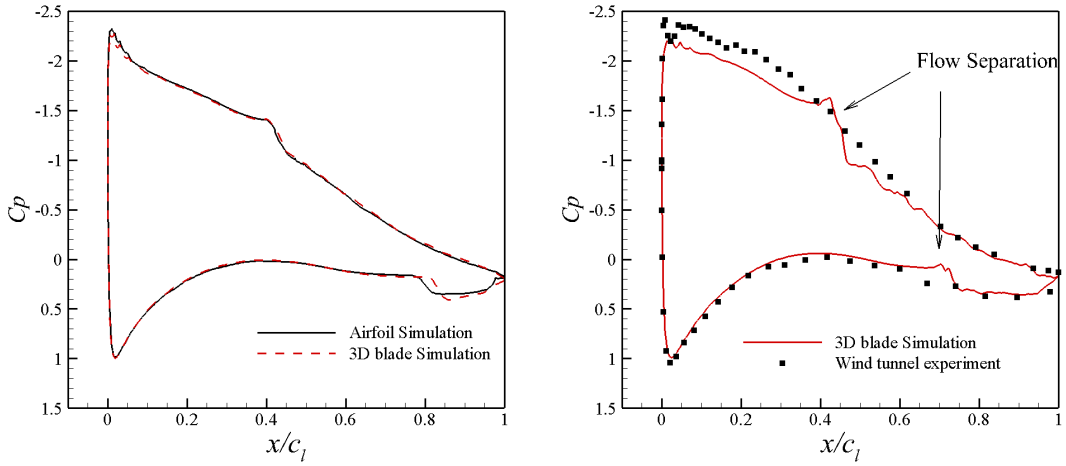

(a) Section1 (y/R = 0.62) (b) Section5 (y/R = 0.47)

Figure 4: Comparison of pressure coefficients of 3D simulation, Airfoil simulation and wind tunnel measurement

plateau in the experimental C_p. As mentioned earlier, the wind tunnel test's Reynolds' number is larger than that in the numerical simulation. Together with free-stream turbulence, the boundary layer transition happens earlier in the experiment. After the transition, the flow re-attaches and there is no separation.

Figure 5 compares the boundary layer velocity profiles of 3D and airfoil simulations. The 3D simulation profiles are at $y_0 = 25.24m$, where the section shape is the same as the airfoil case. The two simulations' streamwise velocity agrees surprisingly well at different locations for both pressure and suction side. The boundary layer flows are laminar at all the locations except for the location $x/c = 0.6$ on the suction side, which is turbulent flow. From the leading edge towards the trailing edge, the laminar boundary layer becomes thicker and the separation begins to develop. However, the separations on both sides are very weak.

In laminar region, the cross-flow velocities of the airfoil simulation are zero since there is no span-wise fluid motion. As a contrast, although the cross-flow velocities are very small, they are not exactly zero for the 3D rotating blade result. Outside boundary layer (inviscid flow region), the radial velocity is positive near the leading edge ($x/c = 0.2$), where the azimuthal velocity decreases because of stagnation point. Near the maximum chord location on suction side ($x/c = 0.4$), because the azimuthal velocity is larger than incoming flow, the Coriolis force outperforms centrifugal force and pull the fluid inward, and the radial velocity is slightly negative.

The radial velocities inside boundary layer are typical cross-flow profiles, i.e., the maximum velocity appears inside the boundary layer. So an inflectional point exists and the flow is inherently unstable. On the suction side, the radial velocity is small near the leading edge, where the flow is fully attached. It progressively increases until reaching its maximum value ($U_r = 0.2$) just before the separation bubble ($x/c = 0.4$).

However, the largest radial velocity is lower than 5% of the corresponding streamwise velocity. Although the cross-flow profile is inherently unstable, its magnitude must be large enough to overcome the viscous effect. In rotating disk and swept wing boundary layers, the cross-flow velocity has to reach $10\% - 20\%$ of the streamwise velocity to intrigue cross-flow transition. Furthermore, the cross-flow component has to maintain a rather long distance to let the disturbance grow. The current result shows that cross-flow transition is unlikely to happen

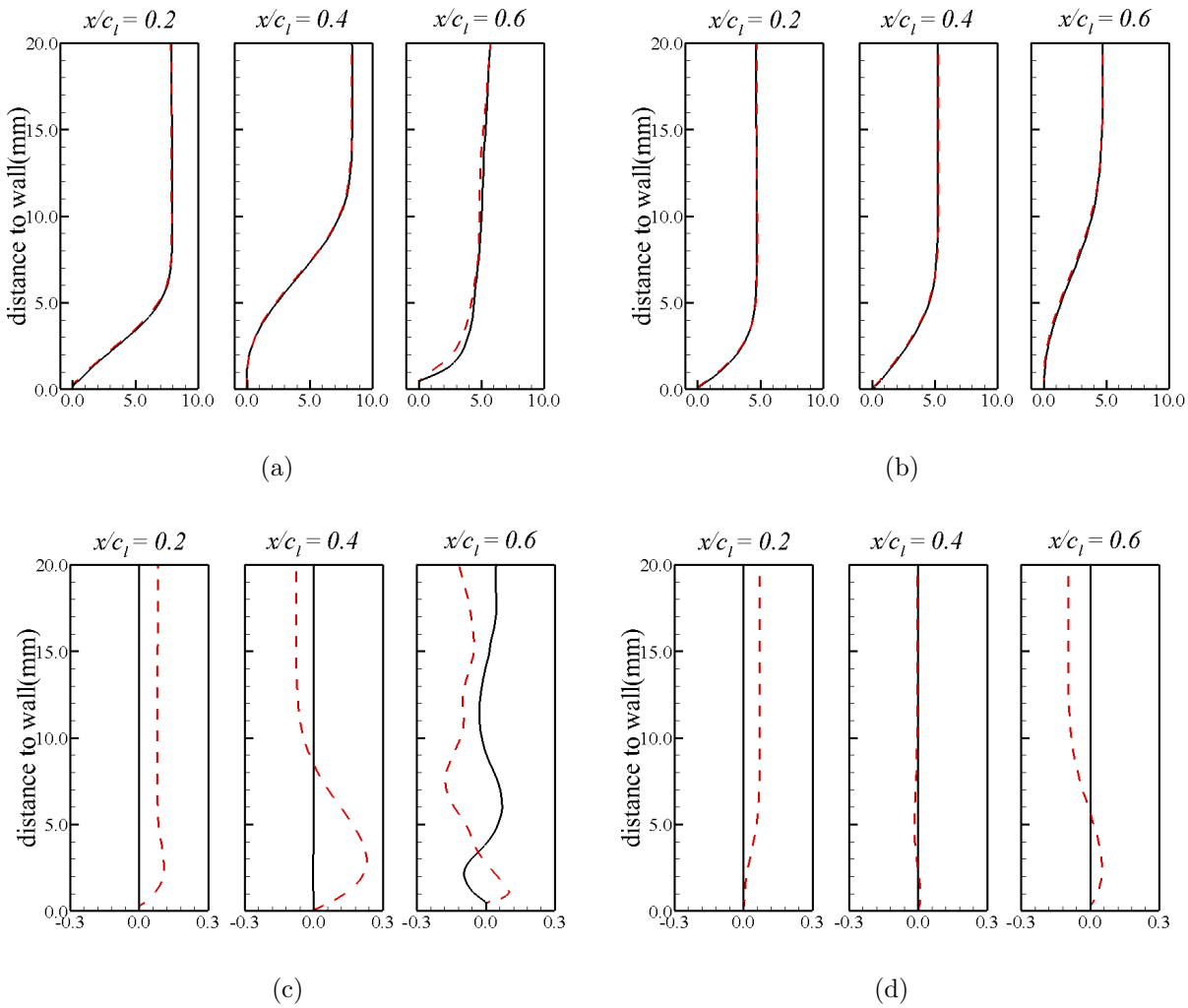

Figure 5: Velocity profile - - - - -3D rotating blade ——Airfoil (a) Streamwise velocity, Suction side (b) Streamwise velocity, Pressure side (c) Cross-flow velocity, Suction side (d) Cross-flow velocity, Pressure side

in rotating HAWT blade since cross-flow's magnitude is too small and it is restricted to the separation region which is quite short.

3.2. Boundary layer instability and transition

Figure 6 gives an overall view of coherent structures at the suction side of the blade. The first noticeable feature is the span-wise streaks around mid-chord of the blade, which are formed by TS waves during laminar-turbulent transition. After the transition, small structures appear in the turbulent region. An interesting feature is that the TS waves are not perfectly aligned to the span-wise direction, i.e., the span-wise wave-number of the TS wave is not zero.

From the coherent structures, the flow field can be divided into three regions. In the two regions near the tip and root, the mesh resolution in y direction is not enough. As a result, the coherent structures show some patterns related to the mesh (please refer to figure 3). For the center portion from around $y = 23$ to $y = 27$, the laminar to turbulent transition and the small turbulent structures are captured.

Figure 7 gives a close-up view of the coherent structures at the suction side of the blade

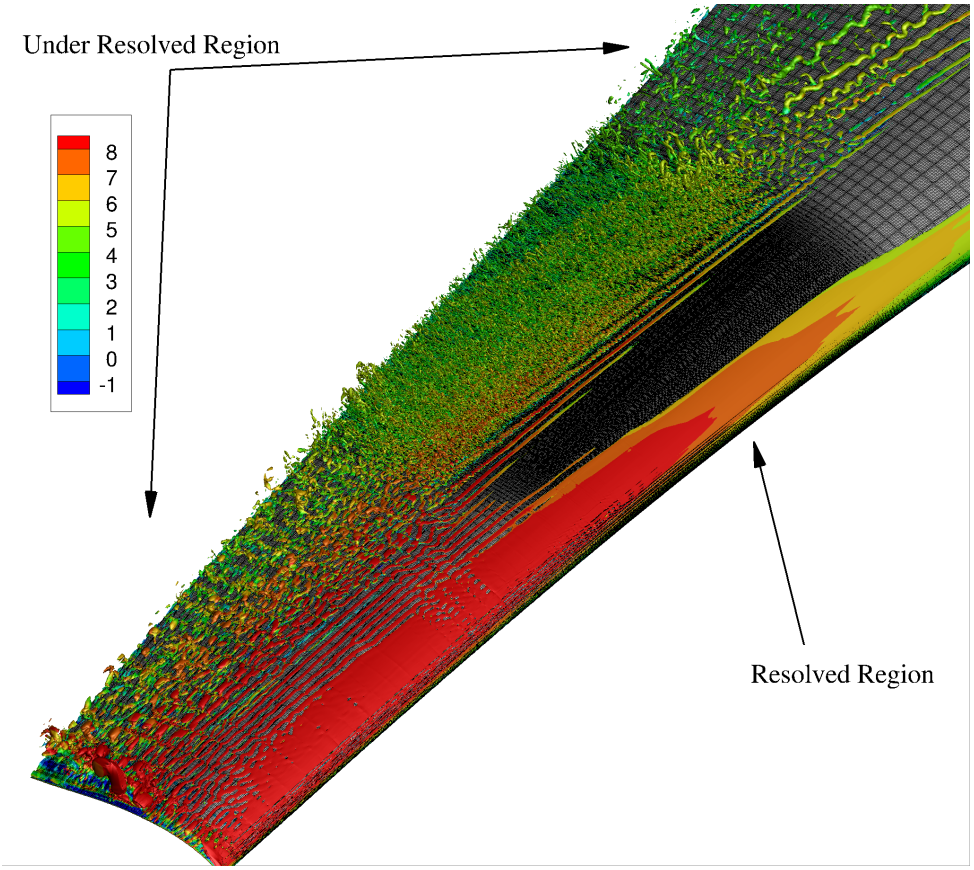

Figure 6: Coherent structure on suction side. Iso-contour of Lambda2, colored by velocity magnitude. (The blade is not to scale)

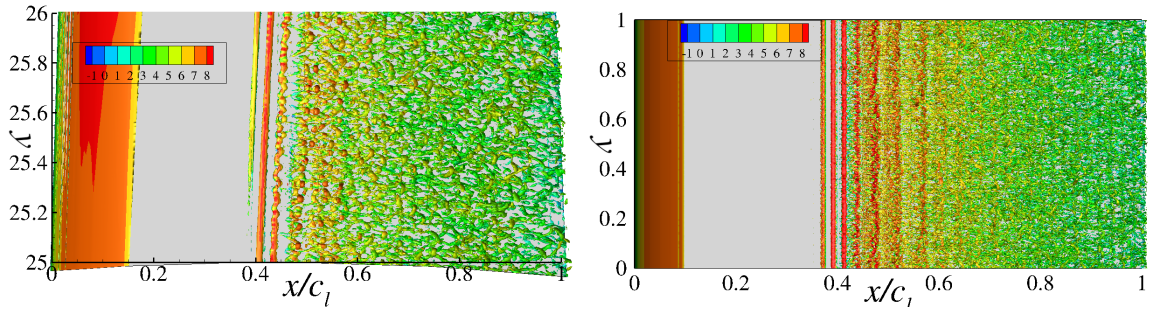

Figure 7: Close up view of coherent structure on suction side (a) 3D rotating blade simulation (b) Airfoil simulation

mid-span as well as the airfoil case. The span-wise streaks are formed by TS waves. 3D and 2D simulations show similar characteristics. In both simulations, the TS waves incept around $x/c_l = 0.4$. They grow quickly and break down after three waves length. After the breakdown, small structures appear and the flow becomes turbulent. For the airfoil simulation, the vortex shedding is also visible. The TS waves in the 2D simulation are 2D (the streak are perfectly aligned to span-wise direction and therefore the span-wise wave number is zero), whereas the

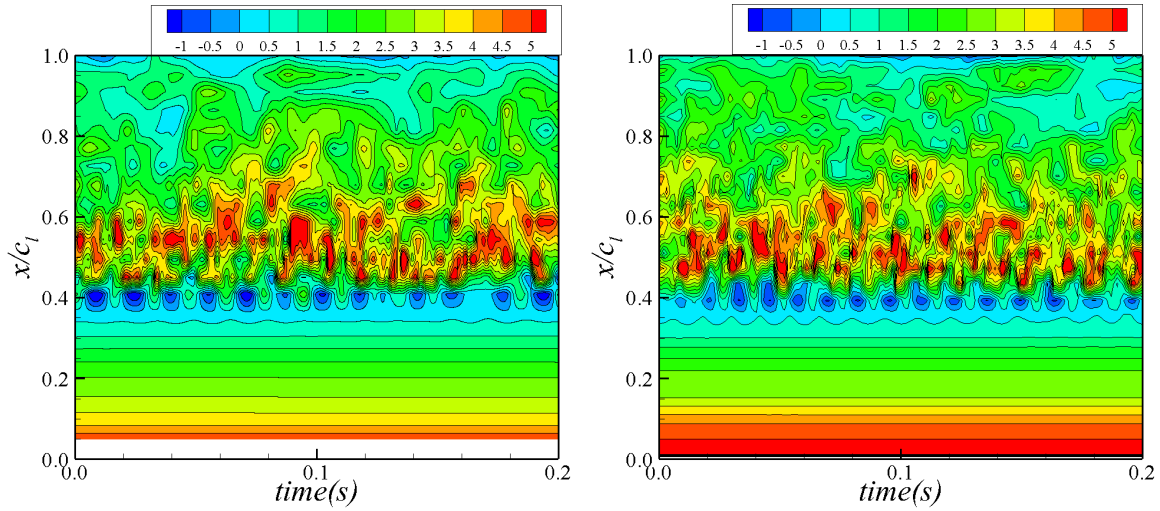

Figure 8: Spatio-temporal diagram of velocity signal (a) azimuthal velocity from 3D simulation at $y = 25.24m$ (the sensors are along Section1) (b) Airfoil simulation (the sensors are located along the mid-span section)

TS waves in 3D rotating blade simulation are 3D waves. As a consequence, one end of TS waves can be seen. However, the small difference between 2D and 3D flow is hardly of any importance from an engineering perspective since the transitional flow region is rather small.

Figure 8 gives the spatio-temporal distribution of streamwise velocity signals recorded during the simulations. Again, the 2D and 3D simulations are similar. The sensors are inside boundary layers and have a roughly constant distance to the wall. As a result, the velocity signal is large near the leading edge since the boundary layer is thin. It decreases until $x/c_l = 0.3$ as the boundary layer grows thicker and thicker. The signals for $x/c_l < 0.3$ do not vary with time since the flow is laminar. Near $x/c_l = 0.35$ the TS wave incepts so the signals become time-periodic. The frequency of 2D and 3D simulation is a little different. 2D TS wave's frequency is around 0.75 Hz and 3D TS wave's frequency is around 0.65 Hz. After the breakdown of TS waves near $x/c_l = 0.40$, the signals become chaotic in both cases.

4. Conclusions and Discussion

In this paper, numerical simulations resolving the boundary layer laminar-turbulent transition are performed for the flow around a rotating LM38.8 blade. A corresponding airfoil simulation with a uniform span is also performed to assess the effect of rotation on this laminar to turbulent transition. It is shown that for the current configuration, the flow field and pressure distribution around the 3D rotating blade can be well approximated by flow around airfoil except for the small radial velocity component.

On the rotating HAWT blade boundary layer, a radial velocity arises because the Coriolis and centrifugal forces cannot keep fluid doing a perfect circular motion. The radial flow is larger in separation bubbles than in attached flow regions. There are two reasons, one is that the Coriolis force acts in the same direction as the centrifugal force; the other one is that the viscous effect is small since the separation bubble is thick. This is in agreement with conclusions from rotating helicopter blades experiments [17].

However, the radial velocity on the rotating HAWT blade is not large enough to affect the flow transition significantly. It is shown that the transition on the rotating blade is caused by

TS wave, which resembles the TS wave on airfoil.

There are several limitations in the current study as well. First, the region investigated does not include tip and root, where the 3D effect is stronger. The parameter chosen in this study (incoming flow and angular velocity) is near-optimal, so there is no massive separation. However, the rotation effect would be more significant when large flow separations exist.

In a wind turbine farm, most wind turbines operate in the wakes of others. At the same time, wind turbines usually operate in atmospheric boundary layers. The incoming flow is rather complex and depends on the upstream turbines, topology of the terrain, and thermal effects. As a result, the transition observed in experiments [10] [14] happens quite near the leading edge and is likely triggered by the bypass transition instead of natural transitions. So another limitation of this study is the uniform inflow and therefore the lack of incoming free stream turbulence. Nevertheless, as it is shown that the effect of rotation on the boundary layer flow is quite small in the attached boundary layer, it is reasonable to believe that the bypass transition on 3D blade is similar to airfoil flow. This study might offer some justifications to study the transition on a HAWT blade using airfoil wind tunnel experiments, as long as the incoming flow condition is well controlled.

Acknowledgments

The first author's PhD is sponsored by China Scholarship Council. Calculation hours for this paper are kindly provided by IDRIS (Grant 2019-[100631]). We would also like to thank DanAero MW project for sharing the blade model and the experimental data.

References

[1] Drela M 1989 Xfoil: An analysis and design system for low reynolds number airfoils *Low Reynolds number aerodynamics* ed Mueller T J (Berlin: Springer-Verlag) pp 1–12
[2] Hansen M O L 2015 *Aerodynamics of wind turbines* (New York: Routledge)
[3] Polat O and Tuncer I 2013 *Procedia Engineering* **61** 28–31
[4] Himmelskamp H 1947 *Profile investigations on a rotating airscrew* (U K: Ministry of Aircraft Production)
[5] Chaviaropoulos P K and Hansen M O L 2000 *J. Fluids Eng.* **122** 330–336
[6] Zhu C, Wang T and Zhong W 2019 *Energies* **12** 1434
[7] Lingwood R J 1995 *Journal of Fluid Mechanics* **299** 17–33
[8] Bosschers J, Montgomerie B, Brand A and van Rooy R P J O M 1996 Influence of blade rotation on the sectional aerodynamics of rotational blades *22nd European Rotorcraft Forum* (London: Royal Aeronautical Society)
[9] Troldborg N, Bak C, Madsen H A and Skrzypinski W R 2013 Danaero mw: final report Tech. rep. DTU Wind Energy
[10] Madsen H, Özçakmak Ö, Bak C, Troldborg N, Sørensen N and Sørensen J 2019 Transition characteristics measured on a 2mw 80m diameter wind turbine rotor in comparison with transition data from wind tunnel measurements *AIAA Scitech 2019 Forum* (AIAA) p 0801
[11] Heister C C 2012 Laminar-turbulent transition prediction for helicopter rotors in hover and forward flight-a rans based investigation of transition mechanism using empirical criteria *38th European Rotorcraft Forum* (Amsterdam)
[12] Hernandez G G M 2012 *Laminar-turbulent transition on wind turbines* Ph.D. thesis DTU Mechanical Engineering
[13] Weiss A 2018 *Investigations of Boundary-layer Transition and Airloads on Rotating Blades* Ph.D. thesis Deutsches Zentrum für Luft-und Raumfahrt
[14] Reichstein T, Schaffarczyk A P, Dollinger C, Balaresque N, Schülein E, Jauch C and Fischer A 2019 *Energies* **12** 2102
[15] Fischer P F, Lottes J W and Kerkemeier S G 2008 Nek5000 17.0.0 URL `https://nek5000.mcs.anl.gov`
[16] Deville M O, Fischer P F and Mund E H 2002 *High-order methods for incompressible fluid flow* (Cambridge: Cambridge university press)
[17] McCroskey W J 1971 Measurements of boundary layer transition, separation and streamline direction on rotating blades Tech. rep. NASA